

Hong-Ou-Mandel interferometry and spectroscopy using entangled photons

Konstantin E. Dorfman¹  , Shahaf Asban², Bing Gu²  & Shaul Mukamel² 

Optical interferometry has been a long-standing setup for characterization of quantum states of light. Both linear and the nonlinear interferences can provide information regarding the light statistics and underlying detail of the light-matter interactions. Here we demonstrate how interferometric detection of nonlinear spectroscopic signals may be used to improve the measurement accuracy of matter susceptibilities. Light-matter interactions change the photon statistics of quantum light, which are encoded in the field correlation functions. Application is made to the Hong-Ou-Mandel two-photon interferometer that reveals entanglement-enhanced resolution that can be achieved with existing optical technology.

¹State Key Laboratory of Precision Spectroscopy, East China Normal University, Shanghai, China. ²Department of Chemistry and Physics & Astronomy, University of California, Irvine, CA, USA. ✉email: dorfman@lps.ecnu.edu.cn

Quantum states of light provide an exciting platform for observing and controlling matter beyond what is possible classically^{1–4}. Quantum states are very sensitive to the external environment, which makes them useful probes of matter. Quantum features of light have long been used in metrology and quantum information^{5,6} while lately there has been a growing activity in utilizing them in spectroscopic applications^{7,8}. Interferometry offers robust detection schemes of quantum light. In this paper, we present a novel spectroscopy based on the Hong-Ou-Mandel (HOM)⁹ two-photon interferometric setup. Observables measured by the interference of two waves depend on two times separated by a delay Δ which can be controlled by the propagation path difference of the mixed waves. The unified picture of second-order and fourth-order interferences in a single interferometer has been demonstrated in ref. ¹⁰. Previous works attempted either to utilize HOM-like measurements to address properties of the beam splitters or the individual emitters¹¹ or utilize four-wave mixing for the quantum light generation¹² and characterization¹³.

Interferometric signals can be recast in terms of moments of the field operators posterior to the interaction with the matter, thereby revealing its statistics. The signal-field operator (see “Methods” and Supplementary Note 1) is given by¹⁴

$$\hat{\mathbf{E}}_s^{(+)}(\mathbf{r}, t) = -i\omega_s \hat{\mathbf{V}}(\mathbf{r}, t), \quad (1)$$

Where ω_s is the signal mode frequency and $\hat{\mathbf{V}}$ is the matter dipole operator. The interferometric setup naturally gives rise to two characteristic timescales and respective length scales. First, the response interval τ_R in which light-matter interaction occurs. It is determined by the pulse envelope, the spatial dimension of the sample, and the response time. Second, is the pulse relative delay interval δT determined by the interference region governed by the interferometer dimensions. Here, we consider the field-matter interaction region to be localized compared to the spatial dimensions of the interferometer. We further consider a sequence of ultrafast coherent excitation pulses—which are classical for all practical purposes—followed by an interaction with the quantum state of light. The interferometer operation mode is shown in Fig. 1: when the pulse interval $c\delta T$ and the maximal response interval of the sample $c\tau_R$, are smaller than the free propagation distance between the sample and the interference-detection location L_p ($L^* \ll L_p$) where $L^* := c\max\{\tau_R, \delta T\}$ —the measured response functions are classical. The response in this regime is highly localized temporally and immediately after the pulse interacts with the sample, the matter degrees of freedom can be

traced out. The excitation and deexcitation period is dominated by the duration of the narrowband envelope of the quantum field given by $c\tau_R$ combined with the pulse delay interval $c\delta T$. The maximal duration of this interval is defined by L^* which is smaller than a few hundred micrometers even for a picosecond pulse which is well within the narrowband region. For example, for a transform-limited Gaussian pulse with central wavelength $\lambda_c = 1064$ nm and pulse duration $\Delta t = 2$ ps which occupies $c\tau_R \approx 600$ μm . Finally, the interferometer length scale denoted L_p specifies the free propagation distance between the incident beams, the beamsplitter, and the detector. Typical interferometer length is in the order of few centimeters which justifies the separation of timescales—considering the interaction interval to be localized around the sample compared with L_p . Moreover, the Rayleigh distance is typically a few meters in this setup, thus one can consider the propagation as unidirectional for all practical purposes. For a femtosecond pulse $c\delta T \propto 10^{-1}$ μm while for a traditional interferometer L_p is in the order of centimeters. In the following we consider short pulses, so that ($L^* \ll L_p$). Trace w.r.t. matter results in the n th order polarization in the external field $P^{(n)}(t) \equiv \hat{\mathbf{V}}(t)_{\{n\}}$ (details are given below). This polarization serves as a source for the signal field. This regime fits experimental setups involving ultrafast pulses ($\delta T \leq 1$ ps). In the opposite regime, $c\tau_R, c\delta T \gg L_p$, the pulse is long enough to create ambiguity in the order of interactions and the arrival of the relatively delayed photons (see Supplementary Notes 2–4 for detailed derivations of this regime). One cannot then trace the matter degrees of freedom prior to the measurement which gives rise to different observables.

In the present work, we combined the interferometric detection (HOM) with wave mixing that involves both classical and quantum light beams to address more complex nonlinear optical processes and the corresponding components of the nonclassical response function. We investigate how the quantum state of light and its statistics are modified by interaction with matter. In particular, we address the following two issues of the quantum nonlinear interferometric spectroscopy. The first issue is regarding the nature of the change of the quantum state and its statistics. The second point investigates the details of the matter information that can be deduced from the change in the statistics of the field. These questions are explored by using an interferometric setup traditionally used to study quantum states of light and now applied for investigation of the matter degrees of freedom via extraction of the matter response functions. We therefore focus on accuracy enhancement of such responses and their deviations from classical susceptibilities.

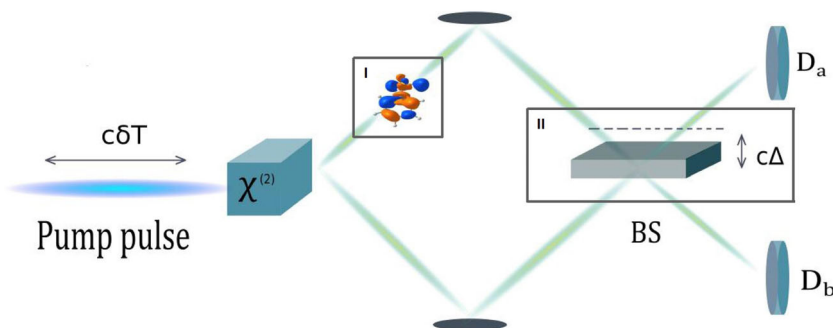


Fig. 1 Interferometric spectroscopy setup. Hong-Ou-Mandel interferometer. A pump beam propagates through a $\chi^{(2)}$ nonlinear crystal. The interaction between field modes mediated through the crystal induces entanglement between two well separated beams of different polarization produced by spontaneous parametric down conversion. One beam interacts with a sample (inset I), while the other propagates in an empty arm. The two beams are finally combined on a beamsplitter (BS) (inset II), and collected in two detectors D_a and D_b . Insets I and II are specified in more detail in Figs. 3 and 4, respectively.

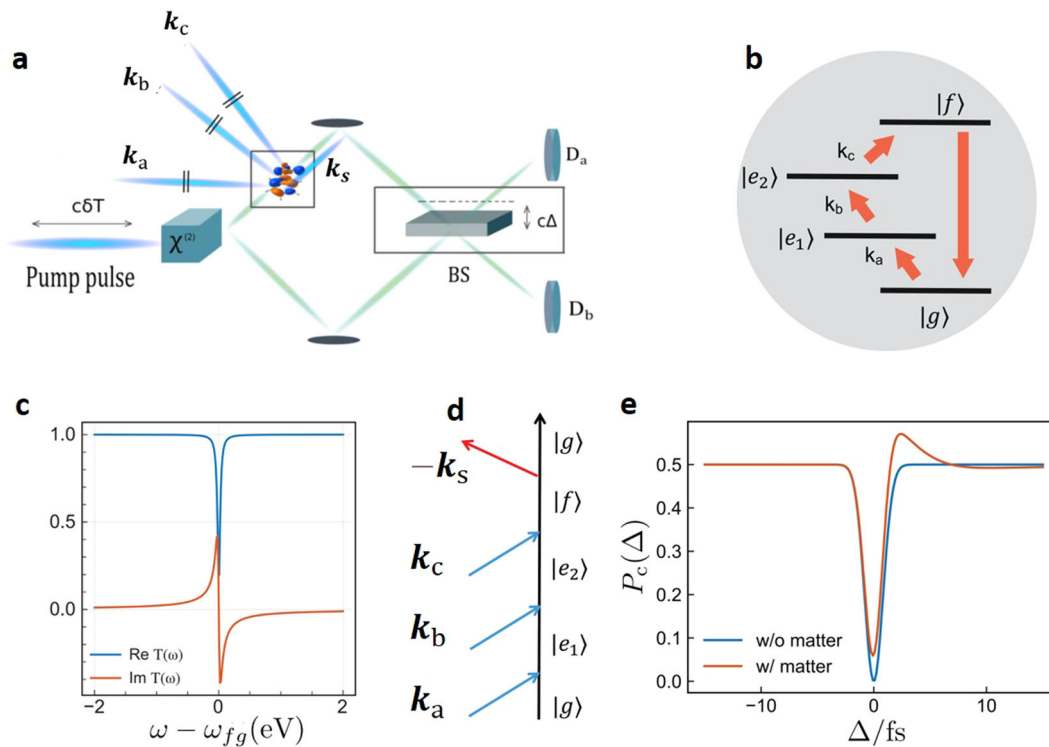


Fig. 2 Hong-Ou-Mandel (HOM) interference signal. An illustration of the variation of the coincidence probability with the optical delay Δ . **a** Level scheme of the model system. **b** Experimental setup based on HOM interferometer combined with four-wave mixing signal. **c** Its transmission function $T(\omega) \equiv 1 - iA_0\chi^{(3)}(\omega)$ (real part—orange line, imaginary part—blue line) Vs the scanned frequency ω_3 at fixed ω_1 and ω_2 . The third-order susceptibility for a multi-level system is computed following ref. ⁹. **d** Schematic diagram representing the main contribution of the third-order susceptibility. **e** Variation of the HOM coincidence counting rates with the optical delay (without matter—blue line, with matter—orange line).

Results and discussion

The proposed experiment combines several conventionally used optical techniques such as four-wave mixing, beam splitting, and Hong-Ou-Mandel (HOM) interferometer, and three-photon absorption spectroscopy. In the following sections, we present each technique independently highlighting the main principle and the underlying theoretical model that will be used to describe each part of the setup. We finally combine both techniques in the setup shown in Fig. 2a and discuss the resulting HOM spectroscopic measurements. In the experimental setup the three classical light beams are combined with the quantum light pulse produced by the parametric down conversion (independently from the classical three pulses). The corresponding level scheme is shown in Fig. 2b. The main goal of the proposed measurement is to use interferometric (HOM-like) detection to investigate the $\chi^{(3)}$ nonlinear susceptibility that combines an absorption of the three classical fields and the transmission of one quantum field shown in Fig. 2c. The corresponding Feynman diagram and HOM signal are shown in Fig. 2d, e, respectively. Unlike the Kerr process which requires high-intensity laser pulses to produce third-order nonlinear response, here we deal with resonant absorption of each of the light beams participating in the four-wave mixing. This nonlinear process is the main focus of our study.

The general third-order nonlinear optical process generates various signals that are well studied in classical light spectroscopy: optical pump-probe, Raman, fluorescence, transient grating, photon echo, and others. Four-wave mixing (FWM) signals play an important role as it allows to have additional control over the field-matter interactions via spatial phase matching. The typical FWM setup shown in Fig. 3 where three beams interacting with

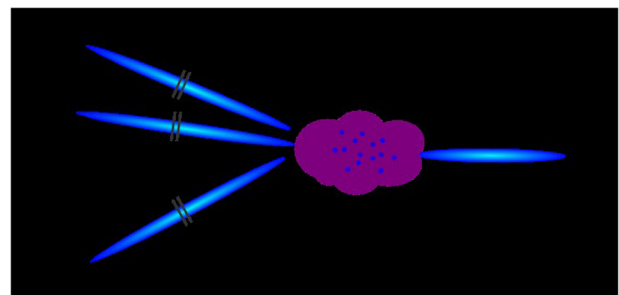


Fig. 3 Four-wave mixing scheme. Inset I in Fig. 1 is shown for a four-wave mixing process. Three incoming waves $\mathbf{k}_1, \mathbf{k}_2, \mathbf{k}_3$ interact with matter. The fourth \mathbf{k}_s mode is the detected signal in the direction dictated by the phase-matching factor $f(\Delta\mathbf{k})$ introduced in Eq. (2).

the material sample generate a fourth beam propagating in the direction governed by one of the eight possible phase-matching conditions. The response functions are obtained by tracing over the matter degrees of freedom. The state of the outgoing field in Fig. 3 is given by tracing Eq. (1) over the matter degrees of freedom $\hat{E}_a^{(+)}(t) \rightarrow \hat{E}_s^{(+)}(t)$,

$$\hat{E}_s^{(+)}(\mathbf{r}, t) = -i\omega_s \sqrt{\frac{\hbar\omega_s}{2\pi}} N f(\Delta\mathbf{k}) \int d\omega \chi^{(3)}(\omega) \hat{a}(\omega) e^{-i\omega t}, \quad (2)$$

where $\chi^{(3)}(\omega) \equiv \chi^{(3)}(-\omega; \omega_3, \omega_2, \omega_1)$ is the third-order susceptibility. We have omitted the three classical incoming wave frequencies for brevity. The matter is modeled by a collection of N homogeneously distributed point-like molecular dipoles at random positions \mathbf{r}_α . Adopting the multipolar coupling Hamiltonian

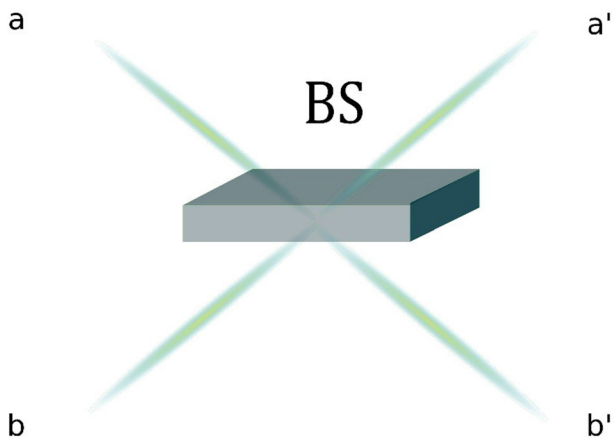


Fig. 4 The beamsplitter. BS of inset II of Fig. 1 is shown with more details. The BS described in Eq. (4), generates a superposition of the incoming fields (plane subscripts) in its output (primed subscripts).

following with rotational averaging we obtain

$$\hat{V}(\mathbf{r}, t)_{\{n\}} = \sum_{\alpha=1}^N \delta(\mathbf{r} - \mathbf{r}_{\alpha}) \hat{V}(t)_{\{n\}} e^{i\mathbf{k}_{\{n\}} \cdot \mathbf{r}}. \quad (3)$$

Here $\{n\}$ denotes averaging with respect to the n th order density operator due to n interacting fields one of which is the photon with the entangled noninteracting counterpart. In this calculation, each of the incoming modes interacts with a single molecule. $f(\Delta\mathbf{k}) = \frac{1}{N} \sum_{\alpha} e^{i\Delta\mathbf{k} \cdot \mathbf{r}_{\alpha}}$ is a geometrical factor that carries the information regarding the distribution of molecules which gives rise to the phase-matching condition when $\Delta\mathbf{k} = 0 = \mathbf{k}_{\{n\}} - \mathbf{k}_s$ and $\mathbf{k}_{\{n\}} = \sum_{i=1}^3 \pm \mathbf{k}_i$ where \mathbf{k}_s is the wavevector of the entangled photon containing the 2^3 phase-matching directions¹⁵. Note that $f(0) = 1$.

The Hong-Ou-Mandel interferometric signal. We next turn to the HOM two-photon interferometer in the presence of matter. The electric field is transformed by the relatively displaced beamsplitter (BS) depicted in Fig. 4 according to

$$\begin{pmatrix} \hat{\mathbf{E}}_{a'}^{(+)}(\omega) \\ \hat{\mathbf{E}}_{b'}^{(+)}(\omega) \end{pmatrix} = \begin{pmatrix} \sqrt{T} & i\sqrt{R}e^{i\omega\Delta} \\ i\sqrt{R}e^{-i\omega\Delta} & \sqrt{T} \end{pmatrix} \begin{pmatrix} \hat{\mathbf{E}}_a^{(+)}(\omega) \\ \hat{\mathbf{E}}_b^{(+)}(\omega) \end{pmatrix}, \quad (4)$$

where the linear phase results in the $\pm\Delta$ relative time delay, corresponding to the $\pm c\Delta$ displacement of the BS. \sqrt{T} and \sqrt{R} are the transmission and reflection coefficients. We focus on the photon coincidence signal depicted in Fig. 1 given by a joint probability to detect one photon in D_a and one photon in D_b separated by delay τ given by

$$\mathcal{N}P_{ab}(\tau) = \left\langle \hat{E}_{a',R}^{(-)}(t) \hat{E}_{b',R}^{(-)}(t + \tau) \hat{E}_{b',L}^{(+)}(t + \tau) \hat{E}_{a',L}^{(+)}(t) \right\rangle, \quad (5)$$

where \mathcal{N} is a normalization factor. We employ the superoperator notation, $O_L A = OA$ and $O_R A = AO$, the superoperator O_{\pm} represents an anti/commutator $O_{\pm} A = OA \pm AO$. Note that the superoperator time ordering T , which is an operator in Liouville space is different from the standard Glauber's normally ordered operators^{7,8}. The plus-minus and the left-right superoperators are linked by a linear transformation. Below we focus on a narrow-band pump. Extension to a broadband pump is outlined in Supplementary Note 2.

The narrowband HOM spectrometer. In their seminal paper, HOM have used the narrowband wavefunction (see Eq. (16) and “Methods”). Following this procedure in path ‘a’ (top branch of the interferometer), a sample composed of many molecules is

placed, and the signal is given by the four-wave mixing setup depicted in Fig. 3.

We focus on the $L^* \ll L_p$ regime, where the spatial extent of the photon wavepacket after the interaction is small compared to the dimensions of the interferometer. Calculating the coincidence count according to Eq. (5) using Eqs. (2) and (15) we obtain,

$$P_{ab}(\tau, \Delta; \{\omega\}_n) = P_0 \left\{ \begin{array}{l} T^2 |C(\tau)|^2 + R^2 |C(2\Delta - \tau)|^2 \\ -RT [C^*(\tau)C(2\Delta - \tau)e^{-i\omega_p(\tau - \Delta)} + c.c.] \end{array} \right\}. \quad (6)$$

Here the convoluted response is given by the functional $C(\tau) = G(\tau)^* \chi^{(3)}(\tau)$, where $G(\tau) = (2\pi)^{-\frac{1}{2}} \int d\omega \Phi(\omega, \omega_p - \omega) e^{-i\omega\tau}$, where the two-photon wavefunction amplitude $\Phi(\omega_a, \omega_b)$ is given by Eq. (15) (see “Methods”); $\chi^{(3)}(\tau) = (2\pi)^{-\frac{1}{2}} \int d\omega \chi^{(3)}(\omega) e^{-i\omega\tau}$ and $\{\omega\}_3 = \omega_1, \omega_2, \omega_3$ are the frequencies of the three classical waves. The pre-factor containing the central frequency and the setup geometry is given by $P_0 = \mathcal{N}^{-1/2} (N\hbar\omega_0^2)^2 |f(\Delta k)|^2$. In the absence of matter, $\chi(t) = \delta(t)$ and we recover the HOM interference⁹ signal. In that case, the extra phase factor that appears in the second term in Eq. (6) can be shifted at the frequency integration by $\omega \rightarrow \omega + \omega_p/2$. When the material sample is added, a reference frequency is set. This can be compensated by equivalently translated matter response. When the coincidence counting is not temporally gated, we obtain the signal by integration over τ ,

$$P_{ab}(\Delta, \{\omega\}_n) = n_0 - \nu \int d\tau \left\{ C^*(\Delta + \tau) C(\Delta - \tau) e^{-i\omega_p\tau} + c.c. \right\}, \quad (7)$$

where $n_0 = P_0(R^2 + T^2) \int d\tau |C(\tau)|^2$, and $\nu = P_0 = P_0 RT$. For large BS displacement $c\Delta$, the overlap term—the second term in the R. H.S. of Eq. (7)—vanishes due to diminishing correlations of the relatively shifted response. It assumes a Wigner function form in the $\{\Delta, \omega_p\}$ space. As Δ is reduced, the overlap term increases, introducing the hallmark dip in the HOM interference pattern. A material sample added in one of the pathways affects the overlap term. Matter information is revealed in Eq. (7) by the variation of the HOM dip with the convoluted response $C(\tau)$ Wigner function as illustrated in Fig. 2e. Note, that the response function $C(\tau)$ is calculated using three classical fields followed by a single-photon field in the last interaction. While it is not unusual that quantum-enhanced performance is dramatically eroded by the loss of a single photon, this is not the case here. Several noise sources can be considered such as losses associated with single-photon sources, non-phase-matched contributions, and imperfect transmission and detection efficiency. First, the proposed setup in the single-photon regime allows overcoming the noise because of the photon correlation measurement. The classical incoming fields contain a large number of photons and are thus insensitive to losses compared to other classical technique. When the single-photon contribution has losses, the signal vanishes due to violation of the phase-matching due to momentum conservation. Second, the improved performance is attributed to the nonclassical correlations between the photon pair, not from their Fock-state characteristics. Contributions to such losses can originate from non-phase-matched signals, like spontaneous emission adding vacuum fluctuations to the transmitted beams. Third, losses occurring after the mixing can be modeled by a beamsplitter with an empty port¹⁶. Recent interferometry: Experiments in the four-wave mixing setup performed in a multiphoton regime¹⁷ indicate the reduction of quantum correlations is proportional to the square of the transmission ratios of the light beam intensities that characterize such losses. Single-photon experiments have substantially lower transmission ratios and are therefore robust

against such losses. Finally, it has been shown that similar biphoton spectroscopy measurements are robust against the external noise at the detection stage such as background thermal radiation¹⁸, even under the signal-to-noise ratio reaches 1/30.

Interferometric detection of $\chi^{(3)}$. We now turn to the setup depicted in Fig. 2a. The molecule is modeled by a four-level system $\{g, e_1, e_2, f\}$ with transition energies $\omega_{e_1g} = E_{e_1} - E_g = 3$ eV, $\omega_{e_2e_1} = 2$ eV, $\omega_{fe_2} = 1$ eV. It undergoes three interactions with classical light pulses with controlled delays, the fourth-interaction is taken to be one photon produced by a parametric down-converted shown in Fig. 2a. The signal with phase matching at $\mathbf{k}_s = \mathbf{k}_a + \mathbf{k}_b + \mathbf{k}_c$ can be generated in the four electronic state system. One can surely select another phase-matching direction, out of the eight possible ones. Each direction contains a different type of material information governed by the set of pathways containing in the corresponding $\chi^{(3)}$ nonlinear susceptibility. The third-order nonlinear susceptibility is calculated using perturbative field-matter interactions according to the diagram in Fig. 2d. Following the general approach outlined in chapter six of ref. ¹⁹. We obtain:

$$\chi^{(3)}(-\omega; \omega_c, \omega_b, \omega_a) = \frac{-\mu_{e_2e_1}\mu_{e_1g}\mu_{e_1g}}{(\omega_a + \omega_b + \omega_c - \omega_g + i\gamma_g)(\omega_a + \omega_b - \omega_{e_2e_1} + i\gamma_{e_2e_1})(\omega_a - \omega_{e_1g} + i\gamma_{e_1g})}, \quad (8)$$

where $\omega = \omega_a + \omega_b + \omega_c$ implies energy conservation and μ_{ij} are transition dipole moments. The nonlinear susceptibility contains one-, two-, and three-photon resonances determined by the transition frequencies ω_{ij} and dephasing rates (linewidth) γ_{ij} , $i, j = g, e_1, e_2, f$.

Figure 2e compares the HOM signal $P_c(\Delta)$ with and without matter. Without matter, the spectrum shows the well-known HOM dip. We consider three classical beams with central frequencies matching the ω_{e_1g} , $\omega_{e_2e_1}$, and ω_{fe_2} . Here $\omega_{mn} = E_m - E_n$ is the transition frequency for $n \rightarrow m$. We assume that the matter-induced modulation of the HOM spectrum measures the susceptibility $\chi^{(3)}(-\omega; \omega_3, \omega_2, \omega_1)$ obtained by scanning ω_3 while ω_1 and ω_2 are fixed. The main contribution to $\chi^{(3)}$ is represented by the ladder diagram shown in Fig. 2d. The sample breaks the time-reversal symmetry $P(\tau) = P(-\tau)$ possessed by the bare HOM dip. Such symmetry is a consequence of the exchange symmetry in the twin-photon wavefunction $\Phi(\omega_1, \omega_2) = \Phi(\omega_2, \omega_1)$. By modulating one arm of the twin-photon, the interaction with matter breaks the exchange symmetry. When absorption can be neglected, the matter acts as a frequency-dependent phase shifter $T(\omega) \equiv e^{i\theta(\omega)}$, the optical delay in the idler beam can compensate the modulation if Δ and θ have the same sign, or further enhance the relative phase difference between the two beams.

The measurement resolution can be controlled by photon entanglement. Figure 5 compares the HOM signal using a nonentangled photon pair (a, b) and highly entangled twin photons (c, d). The two-photon wavefunctions in panels a and c, and the corresponding HOM signals, are shown in panels b and d. The coincidence HOM measurement can reveal the energies and lifetimes of the four electronic levels $\{g, e_1, e_2, f\}$ along with the transition dipoles between the states and relevant coherence dephasing rates. For instance, the f-g coherence dephasing is a crucial parameter that determines the temporal resolution of the coincidence measurement and strongly depends on the state of light. The signal in Fig. 5 is computed by scanning the pump frequency impinging the nonlinear crystal. As shown, the central feature arises at $\frac{\omega}{2} = 6$ eV which matches the transition frequency ω_{fg} . The decay of the signal comes from the finite lifetime of the $|f\rangle \langle g|$ coherence induced by the classical laser pulses. While both classical and quantum light give the resonance frequency, the

temporal resolution that can track the f-g coherence decay is significantly enhanced by using a highly entangled photon pair. This can be understood in a similar way to the two-photon absorption with entangled photons where the product of temporal and spectral resolutions violates the uncertainty relation.

The quantum light statistics is modified by interaction with matter. To understand the nature of the change and the matter information it carries, we have used the HOM interferometric setup which provides information about the state of light after the interaction with matter. Ultrashort pulses can exploit the quantum nature of light in order to increase the measurement accuracy of a classical response function. This was studied in detail for a model system.

Interaction of quantum systems changes their state in the course of light-matter interaction at a single-photon regime^{20–22}. Each interaction enhances the correlation, and the system becomes more inseparable. This may be employed in novel quantum spectroscopic setups, which extract matter information from optical probes. While single-photon states can be easily described in the photon number (Fock) basis, they are less suitable for probing phase-shifts due to number-phase uncertainty^{23,24}. Multiphoton (entangled) states provide a richer playground for improving the temporal resolution imprinted by matter on the optical probe and is the focus of our study. Multimode squeezed states²⁵ may be useful since the number-phase uncertainty can be further tuned in order to reach a desired joint frequency-time resolution.

Methods

Optical signals description. We start with the joint light-matter Hamiltonian,

$$\hat{H} = \hat{H}_\mu + \hat{H}_\phi + \hat{H}_{\mu\phi}, \quad (9)$$

where μ, ϕ represent the matter and electromagnetic field, respectively, and $\hat{H}_{\mu\phi}$ is their coupling. The electric field operator is partitioned into positive and negative frequency components,

$$\hat{\mathbf{E}}(\mathbf{r}, t) = \sum_{s=1}^{n+1} \hat{\mathbf{E}}_s^{(+)}(\mathbf{r}, t) + \hat{\mathbf{E}}_s^{(-)}(\mathbf{r}, t), \quad (10)$$

$$\hat{\mathbf{E}}_s^{(+)}(\mathbf{r}, t) = [\hat{\mathbf{E}}_s^{(-)}(\mathbf{r}, t)]^\dagger,$$

where the sum over s runs over the modes participating in the wave-mixing experiment, the positive frequency component (h.c. of the negative counterpart) in the continuum limit is expressed in the slowly varying amplitude approximation,

$$\hat{\mathbf{E}}_s^{(+)}(\mathbf{r}, t) = \left(\frac{\hbar\omega_s}{2\pi}\right)^{\frac{1}{2}} e^{i\mathbf{k}_s \cdot \mathbf{r}} \int d\omega \hat{a}_s(\omega) e^{-i\omega t} \quad (11)$$

with the canonical bosonic commutation relations $[a_s(t), a_{s'}^\dagger(t')] = \delta_{ss'} \delta(t - t')$.

Given the dipole operator $\hat{\mu} = \hat{V} + \hat{V}^\dagger$, the light-matter interaction in the rotating wave approximation (RWA) is given by,

$$\hat{H}_{\mu\phi} = \hat{\mathbf{E}}^{(-)}(\mathbf{r}, t) \hat{V}(\mathbf{r}, t) + \hat{\mathbf{E}}^{(+)}(\mathbf{r}, t) \hat{V}^\dagger(\mathbf{r}, t), \quad (12)$$

which associates absorption of a photon with dipole excitation and emission with deexcitation. We shall solve the equation of motion of the field in the interaction picture,

$$\frac{d}{dt} \hat{\mathbf{E}}_s^{(+)}(\mathbf{r}, t) = -\frac{i}{\hbar} [\hat{\mathbf{E}}_s^{(+)}(\mathbf{r}, t), \hat{H}_{\mu\phi}(\mathbf{r}, t)]. \quad (13)$$

The entangled two-photon wavefunction. We next present the general form of the entangled two-photon wavefunction. Equations (15), (16), and (S10) are then used for two limiting cases of narrowband and broadband generating pulses. The wavefunction of frequency-entangled photons, generated by a parametric down-conversion (PDC) is given by^{26,27},

$$|\psi\rangle = \int d\omega_a d\omega_b \Phi(\omega_a, \omega_b) a^\dagger(\omega_a) b^\dagger(\omega_b) |0_a, 0_b\rangle, \quad (14)$$

where $\Phi(\omega_a, \omega_b)$ is the two-photon amplitude and $a^\dagger(\omega)$ and $b^\dagger(\omega)$ are creation operators for the two modes. Here ω_a/c and ω_b/c correspond to the projections of the wavevectors along the crystal length, where c is a speed of light. These operators obey boson commutation relations $[a(\omega), a(\omega')] = [b(\omega), b(\omega')] = [a(\omega), b^\dagger(\omega')] = 0$ and $[a(\omega), a^\dagger(\omega')] = [b(\omega), b^\dagger(\omega')] = \delta(\omega - \omega')$. For a type II phase-matched PDC process generated by a broadband pulse, the amplitude is given by pump envelope

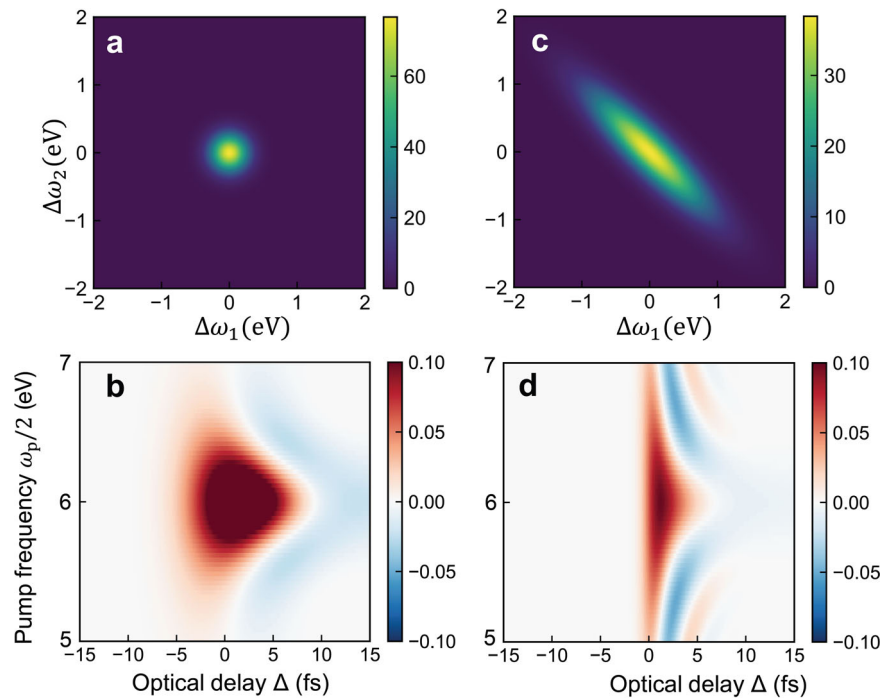


Fig. 5 2D photon coincidence counting signal. $P_{ab}(\Delta, \omega_p)$ [Eq. (7)] for the model system of Fig. 2b. The pump frequency ω_p creating the entangled photon pair and the optical delay between two arms are varied. We approximate a sinc-shape of the two-photon wavefunction by a Gaussian for simplified frequency integration: $\Phi(\omega_1, \omega_2) = (2\pi\sigma_+\sigma_-)^{-1/2} \exp[-(\omega_1 + \omega_2 - \omega_p)^2 / (16\sigma_+^2)] \exp[-(\omega_1 - \omega_2)^2 / (4\sigma_-^2)]$. **a** Two-photon wavefunction of unentangled photons with $\sigma_+ = 0.1$ eV, $\sigma_- = 0.2$ eV. **b** The Hong-Ou-Mandel (HOM) spectrum using the two-photon state in **(a)**. **c** Two-photon wavefunction of highly entangled twin photons with energy anti-correlation. Here $\sigma_+ = 0.1$ eV, $\sigma_- = 0.8$ eV. **d** The HOM spectrum obtained using the twin-photon state in **(c)**. The resolution is clearly enhanced by the entangled photon pair.

multiplied by the phase-matching factor

$$\Phi(\omega_a, \omega_b) = \alpha(\omega_a, \omega_b)\varphi(\omega_a, \omega_b). \quad (15)$$

The Gaussian envelope is given by $\alpha(\omega_a, \omega_b) = (2\pi\sigma_p^2)^{-1/2} \exp[-(\omega_a + \omega_b - \omega_p)^2 / (2\sigma_p^2)]$, which is inherited from the pump pulse centered around ω_p with σ_p bandwidth. The phase-matching condition is included in the two-photon state amplitude²⁶ $\varphi(\omega_a, \omega_b) = \text{sinc}\left\{L_c\left[(\omega_a - \frac{\omega_p}{2})(k'_a - k'_p) + (\omega_b - \frac{\omega_p}{2})(k'_b - k'_p)\right]\right\}$. Here L_c is the length of the generating nonlinear crystal, $k'_{a,b}$ are the inverse group velocity at half pump frequency $\frac{\omega_p}{2}$ and k'_p is the corresponding velocity at the central frequency ω_p .

There are two limiting cases for this wavefunction. One is mostly used for ultrafast pulses resulting in wide bandwidth pump. In this case, a Schmidt decomposition to pulse-modes is useful. The other is narrowband limit in which the width of the pump envelope σ_p^2 is set to zero. For a narrowband pump pulse, $\alpha(\omega_a, \omega_b) \rightarrow \delta(\omega_a + \omega_b - \omega_p)$, and the conjugate temporal profile $\delta T = \sigma_p^{-1}$ is therefore large. The two-photon wavefunction then takes the form,

$$|\psi\rangle_{nb} = \int d\omega \text{sinc}\left[\left(\omega - \frac{\omega_p}{2}\right)T_a + \left(\frac{\omega_p}{2} - \omega\right)T_b\right] |\omega\rangle_a |\omega_p - \omega\rangle_b \quad (16)$$

where we have defined the time variables $T_{a/b} = (k'_{a/b} - k'_p)L_c$. By shifting the frequency variables, we obtain

$$|\psi\rangle_{nb} = \int d\omega \text{sinc}[\omega T_{\text{ent}}] \left| \omega + \frac{\omega_p}{2} \right\rangle_a \left| \frac{\omega_p}{2} - \omega \right\rangle_b \quad (17)$$

where $T_{\text{ent}} = T_a - T_b$ is the entanglement time. Note, that the wavefunction in Eq. (15) does not generally possess exchange symmetry, since the twin state represents the state of the field modes (amplitudes), which can be distinguished by, e.g., group velocity dispersion, polarization etc. In the same time, Eq. (16) yields a simplified expression originating from the narrowband pump pulse, where overlapping modes result in the exchange symmetry of the wavefunction typical for the HOM experiment. A more general treatment of the photon wavefunctions is discussed in ref. ²⁸.

Data availability

The authors declare that full theoretical details are available in the Supplementary Information. All raw data that support the findings in this study are available from the corresponding authors upon request.

Received: 3 October 2020; Accepted: 1 February 2021;

Published online: 11 March 2021

References

- Mukamel, S. et al. Roadmap on quantum light spectroscopy. *J. Phys. B: Mol. Opt. Phys.* **53**, 072002 (2020).
- Kalashnikov, D. A., Paterova, A. V., Kuli, S. P. & Krivitsky, L. A. Infrared spectroscopy with visible light. *Nat. Photonics* **10**, 98–101 (2016).
- Hempel, C. et al. Entanglement-enhanced detection of single-photon scattering events. *Nat. Photonics* **7**, 630–633 (2013).
- León-Montiel, R. D. J., Svozilík, J., Torres, J. P. & U'Ren, A. B. Temperature-controlled entangled-photon absorption spectroscopy. *Phys. Rev. Lett.* **123**, 023601 (2019).
- Parker, S., Bose, S. & Plenio, M. B. Entanglement quantification and purification in continuous-variable systems. *Phys. Rev. A* **61**, 032305 (2000).
- Huang, H. & Eberly, J. H. Correlations and one-quantum pulse shapes in photon pair generation. *J. Mod. Opt.* **40**, 915–930 (1993).
- Dorfman, K. E., Schlawin, F. & Mukamel, S. Nonlinear optical signals and spectroscopy with quantum light. *Rev. Mod. Phys.* **88**, 045008 (2016).
- Asban, S., Dorfman, K. E. & Mukamel, S. Quantum phase-sensitive diffraction and imaging using entangled photons. *PNAS* **116**, 11673–11678 (2019).
- Hong, C. K., Ou, Z. Y. & Mandel, L. Measurement of subpicosecond time intervals between two photons by interference. *Phys. Rev. Lett.* **59**, 2044–2046 (1987).
- Qiu, J., Zhang, Y. S., Xiang, G. Y., Han, S. S. & Gui, Y. Z. Unified view of the second-order and the fourth-order interferences in a single interferometer. *Opt. Commun.* **336**, 9–13 (2015).
- Dorfman, K. E. & Mukamel, S. Indistinguishability and correlations of photons generated by quantum emitters undergoing spectral diffusion. *Sci. Rep.* **4**, 3996 (2014).
- Yang, Z., Saurabh, P., Schlawin, F., Mukamel, S. & Dorfman, K. E. Multidimensional four-wave-mixing spectroscopy with squeezed light. *Appl. Phys. Lett.* **116**, 244001 (2020).
- Lvovsky, A. I. & Raymer, M. G. Continuous-variable optical quantum-state tomography. *Rev. Mod. Phys.* **81**, 299–332 (2009).

14. Mollow, B. R. Resonant scattering of radiation from collision-damped two-level systems. *Phys. Rev. A* **2**, 76 (1970).
15. Roslyak, O. & Mukamel, S. A unified description of sum frequency generation, parametric down conversion and two-photon fluorescence. *Mol. Phys.* **107**, 265–280 (2009).
16. Bachor, H. A. & Ralph, T. C. A *Guide to Experiments in Quantum Optics* (Wiley-VCH, 2004).
17. Wang, L., Wang, H., Li, S., Wang, Y. & Jing, J. Phase-sensitive cascaded four-wave-mixing processes for generating three quantum correlated beams. *Phys. Rev. A* **95**, 013811 (2017).
18. Kalachev, A. A. et al. Biphoton spectroscopy of YAG:Er³⁺ crystal. *Las. Phys.* **4**, 722 (2006).
19. Mukamel, S. *Principles of Nonlinear Optical Spectroscopy* (Oxford University Press, 1995).
20. Crisp, M. D. Propagation of small-area pulses of coherent light through a resonant medium. *Phys. Rev. A* **1**, 1604 (1970).
21. Eberly, J. H. Optical pulse and pulse-train propagation in a resonant medium. *Phys. Rev. Lett.* **22**, 760 (1969).
22. Kalashnikov, D. A. et al. Quantum interference in the presence of a resonant medium. *Sci. Rep.* **7**, 11444 (2017).
23. Martin, L. S., Livingston, W. P., Hacothen-Gourgy, S., Wiseman, H. M. & Siddiqi, I. *arXiv* **1906**, 07274 (2019).
24. Busch, P., Lahti, P., Pellonpää, J.-P. & Ylänne, K. Are number and phase complementary observables? *J. Phys. A: Math. Gen.* **34**, 5923–5935 (2001).
25. Andersen, U. L., Gehring, T., Marquardt, C. & Leuchs, G. 30 years of squeezed light generation. *Phys. Scr.* **91**, 053001 (2016).
26. Law, C. K., Walmsley, I. A. & Eberly, J. H. Continuous frequency entanglement: effective finite hilbert space and entropy control. *Phys. Rev. Lett.* **84**, 5304–5307 (2000).
27. Branning, D., Grice, W. P., Erdmann, R. & Walmsley, I. A. Engineering the indistinguishability and entanglement of two photons. *Phys. Rev. Lett.* **83**, 955–958 (1999).
28. Smith, B. J. & Raymer, M. G. Photon wave functions, wave-packet quantization of light, and coherence theory. *N. J. Phys.* **9**, 414 (2007).

Acknowledgements

K.E.D. acknowledges the support from National Science Foundation of China (No. 11934011), Zijiang Endowed Young Scholar Fund, East China Normal University, and

Overseas Expertise Introduction Project for Discipline Innovation (111 Project, B12024). S.M. gratefully acknowledges the support of the National Science Foundation through Grant No. CHE-1953045.

Author contributions

K.D., S.A., B.G. and S.M. contributed to the design and writing of the paper. B.G. performed the simulations.

Competing interests

The authors declare no competing interests.

Additional information

Supplementary information The online version contains supplementary material available at <https://doi.org/10.1038/s42005-021-00542-2>.

Correspondence and requests for materials should be addressed to K.E.D.

Reprints and permission information is available at <http://www.nature.com/reprints>

Publisher's note Springer Nature remains neutral with regard to jurisdictional claims in published maps and institutional affiliations.



Open Access This article is licensed under a Creative Commons Attribution 4.0 International License, which permits use, sharing, adaptation, distribution and reproduction in any medium or format, as long as you give appropriate credit to the original author(s) and the source, provide a link to the Creative Commons license, and indicate if changes were made. The images or other third party material in this article are included in the article's Creative Commons license, unless indicated otherwise in a credit line to the material. If material is not included in the article's Creative Commons license and your intended use is not permitted by statutory regulation or exceeds the permitted use, you will need to obtain permission directly from the copyright holder. To view a copy of this license, visit <http://creativecommons.org/licenses/by/4.0/>.

© The Author(s) 2021